Te incorporation and activation as n-type dopant in self-catalyzed GaAs nanowires

Hakkarainen, Teemu; Piton, Marcelo Rizzo; Fiordaliso, Elisabetta Maria; Leshchenko, Egor D.; Koelling, Sebastian; Bettini, Jefferson; Avanco Galeti, Helder Vinicius; Koivusalo, Eero; Gobato, Yara Galva; Rodrigues, Ariano de Giovanni

Total number of authors:
15

Published in:
Physical Review Materials

Link to article, DOI:
10.1103/PhysRevMaterials.3.086001

Publication date:
2019

Document Version
Publisher's PDF, also known as Version of record

Te incorporation and activation as *n*-type dopant in self-catalyzed GaAs nanowires

Teemu Hakkarainen,[1,*] Marcelo Rizzo Piton,[1,2] Elisabetta Maria Fiordaliso,[3] Egor D. Leshchenko,[4] Sebastian Koelling,[5] Jefferson Bettini,[6] Helder Vinicius Avanço Galeti,[7] Eero Koivusalo,[1] Yara Galvão Gobato,[2,8] Ariano de Giovanni Rodrigues,[2] Donald Lupo,[9] Paul M. Koenraad,[5] Edson Roberto Leite,[6] Vladimir G. Dubrovskii,[10] and Mircea Guina[1]

[1]*Optoelectronics Research Centre, Physics Unit, Tampere University, Korkeakoulunkatu 3, 33720 Tampere, Finland*

[2]*Physics Department, Federal University of São Carlos, 13565-905 São Carlos SP, Brazil*

[3]*National Center for Nano Fabrication and Characterization (Nanolab), Technical University of Denmark, Fysikvej, 2800 Lyngby, Denmark*

[4]*Solid State Physics and NanoLund, Lund University, Box 118, S-22100 Lund, Sweden*

[5]*Photonics and Semiconductor Nanophysics, Department of Applied Physics, Eindhoven University of Technology, Eindhoven 5600 MB, The Netherlands*

[6]*Brazilian Nanotechnology National Laboratory (LNNano)—CNPEM, R. Giuseppe Máximo Scolfaro, 10000 Campinas SP, Brazil*

[7]*Electrical Engineering Department, Federal University of São Carlos, 13565-905 São Carlos SP, Brazil*

[8]*High Field Magnet Laboratory, Radboud University, 6525 ED Nijmegen, Netherlands*

[9]*Laboratory of Electronics and Communications Engineering, Tampere University, Korkeakoulunkatu 3, FI-33720 Tampere, Finland*

[10]*ITMO University, Kronverkskiy pr. 49, 197101 Saint Petersburg, Russia*

(Received 7 March 2019; revised manuscript received 10 June 2019; published 5 August 2019)

Dopant atoms can be incorporated into nanowires either via the vapor-liquid-solid mechanism through the catalyst droplet or by the vapor-solid growth on the sidewalls. Si is a typical *n*-type dopant for GaAs, but in nanowires it often suffers from a strongly amphoteric nature in the vapor-liquid-solid process. This issue can be avoided by using Te, which is a promising but less common alternative for *n*-type doping of GaAs nanowires. Here, we present a detailed investigation of Te-doped self-catalyzed GaAs nanowires. We use several complementary experimental techniques, such as atom probe tomography, off-axis electron holography, micro-Raman spectroscopy, and single-nanowire transport characterization, to assess the Te concentration, the free-electron concentration, and the built-in potential in Te-doped GaAs nanowires. By combing the experimental results with a theoretical model, we show that Te atoms are mainly incorporated by the vapor-liquid-solid process through the Ga droplet, which leads to both axial and radial dopant gradients due to Te diffusion inside the nanowires and competition between axial elongation and radial growth of nanowires. Furthermore, by comparing the free-electron concentration from Raman spectroscopy and the Te-atom concentrations from atom probe tomography, we show that the activation of Te donor atoms is 100% at a doping level of 4×10^{18} cm^{-3}, which is a significant result in terms of future device applications.

DOI: 10.1103/PhysRevMaterials.3.086001

I. INTRODUCTION

Semiconductor nanowires (NWs) are considered to be one of the most promising building blocks for nanoscience and nanotechnology [1]. This is to a large extent due to the one-dimensional geometry of NWs, which allows for combining dissimilar semiconductor materials in heterostructures and growing them on lattice-mismatched substrates. In particular, self-catalyzed vapor-liquid-solid (VLS) NW growth [2,3] enables direct epitaxial integration of high quality III-V semiconductor materials on Si substrates without the use of foreign metal catalysts such as Au, which may form unwanted defect states [4]. Exploitation of NWs in LEDs [5,6], solar cells [7,8], photodetectors [9], and other optoelectronic devices requires a controllable methodology for doping. Consequently, significant efforts have been put into the investigation of the NW doping process [10]. A specific feature of the VLS process is that dopants can incorporate either through the catalyst droplet or via the vapor-solid (VS) growth on the NW sidewalls. In the case of Si, which is routinely used as an *n*-type dopant in planar GaAs-based optoelectronic technologies, the VS incorporation results in *n*-type doping, while strongly amphoteric behavior is observed for the VLS mechanism, leading to *p*-type doping [11,12]. Recently, the group-VI element Te has emerged as a promising candidate for *n*-type doping of III-V NWs. Te occupies anion sites [13] and acts as an effective *n*-type dopant in several VS grown III-V alloys, such as GaAs [14], InGaAs [15], GaAsSb, and GaSb [16]. While Te has successfully been used for *n*-type doping of Au-catalyzed [17,18] and self-catalyzed GaAs [19–21] NWs, a full understanding of the Te incorporation into VLS NWs is still largely missing.

Consequently, here we report a detailed investigation of Te incorporation in the self-catalyzed growth of GaAs NWs on Si substrates. We combine a number of complementary experimental techniques including atom probe tomography (APT), off-axis electron holography, micro-Raman spectroscopy, and single-NW transport characterization. This allows us to assess the achieved Te doping level, the free-electron

*Corresponding author: teemu.hakkarainen@tuni.fi

concentrations, and spatial concentration gradients. A theoretical model is proposed for Te incorporation via the VLS mechanism, which explains the observed axial and radial dopant gradients in NWs. Furthermore, we show that 100% Te dopant activation can be achieved at a concentration of $4 \times 10^{18}\,\mathrm{cm}^{-3}$, which is a significant result for future device applications.

II. EXPERIMENTAL DETAILS

A. Nanowire growth

The investigated self-catalyzed GaAs NWs were grown by solid-source molecular-beam epitaxy (MBE) on lithography-free oxide patterns fabricated on *p*-Si(111) substrates by droplet epitaxy and spontaneous oxidation, as described in detail in Ref. [22]. The nucleation site density of the used template was $4.4 \times 10^{7}\,\mathrm{cm}^{-2}$. Prior to NW growth, the samples were annealed for 30 min without any fluxes at 660 °C, as determined by a pyrometer. The annealing was followed by 40-s Ga predeposition at the growth temperature of 640 °C, with the Ga flux corresponding to 0.3-μm/h planar growth rate on GaAs(100) substrate. The NW growth was then initiated by providing As_2 with a V/III beam equivalent pressure (BEP) ratio of 9. Te was provided from a GaTe cell, with a nominal dopant concentration of $2.0 \times 10^{19}\,\mathrm{cm}^{-3}$. The doping levels were calibrated based on Hall measurements of planar Te-doped GaAs samples grown on semi-insulating GaAs(100) substrates. Te-doped GaAs NWs were grown for 60 min. The growth was terminated by simultaneously switching off all the fluxes and rapidly cooling down the sample. Two samples with undoped reference NWs were also grown using the same process without Te flux. The growth times for the reference NWs were 60 and 80 min. Additionally, a Te-doped sample with an undoped AlGaAs shell was grown for electron holography and APT measurements. These *n*-GaAs/*i*-AlGaAs core-shell NWs were grown on the same template material as the bare NWs. Te-doped GaAs cores were grown similarly to the bare NWs, after which the NW growth was terminated under a constant As flux by ramping down the temperature to 560 °C during a 5-min growth interrupt. The nominal shell composition was $Al_{0.33}Ga_{0.67}As$ and the planar growth rate was $0.45\,\mu\mathrm{m/h}$. A higher V/III BEP ratio of 17 was used for the shell growth. The nominal AlGaAs shell thickness was 20 nm, accounting for the flux angles and sample rotation.

B. Atom probe tomography

Samples for APT measurements of NWs were prepared using the method described in Ref. [23]. APT was carried out using a LEAP 4000X-HR from Cameca. The system is equipped with a laser generating picosecond pulses at a wavelength of 355 nm. For the analysis, all samples were cooled down to a temperature of 20 K and then either laser pulses with pulse energies between 1.2 and 2 pJ or voltage pulses with a pulse fraction of 40% were applied to the sample. The acquired data were reconstructed using IVAS 3.6.8.

In the AlGaAs/GaAs core/shell structures analyzed in this paper, the different materials exposed at the NW surface show different evaporation behavior. This results in artifacts during the projection that are discussed in detail in Ref. [24]. As in Ref. [24], the AlGaAs shell severely compresses the GaAs core when field evaporation is assisted by laser pulses. However, no artifacts are observed when voltage pulses are utilized. Hence, the analyses of the bare Te-doped GaAs NWs were carried out with laser pulses, while the analyses of core-shell structures were carried out with voltage pulses.

C. Off-axis electron holography

Cross-sectional samples for off-axis electron holography were prepared by focused ion beam (FIB) from the lower and upper parts of *n*-GaAs-AlGaAs core-shell NWs, as shown in Figs. S5(a) and S6(a) in the Supplemental Material [25], using a FEI Helios dual beam microscope equipped with a micromanipulator for *in situ* liftout. The NWs were coated by Pt prior to the FIB cut. Holograms were recorded using a FEI Titan 80-300ST field emission gun transmission electron microscope, operating at 120 kV and equipped with a rotatable Möllenstedt biprism.

D. Raman spectroscopy

Raman spectra of undoped and Te-doped GaAs NWs were measured from the as-grown samples using a Renishaw inVia Raman Microscope equipped with a 100X (NA = 0.85) objective lens. The NW density on the substrate was low enough to focus a ∼1-μm excitation spot of a 532-nm excitation laser on a single NW, as shown in Fig. S7 in the Supplemental Material [25]. The measurements were performed in the backscattering geometry with the excitation beam parallel to the NW growth axis. The linear polarization of the excitation laser was set perpendicular to the NW axis and the detection of the scattered intensity was unpolarized. The short depth of field of the confocal arrangement together with vertical scanning using a *z* piezo was employed for probing the Raman scattering from different positions along the NW axis. The intensity of the Si optical modes at $\sim 520\,\mathrm{cm}^{-1}$ was used for determining the *z* position corresponding to the NW-substrate interface.

E. Device processing for transport characterization

The Te-doped NWs used for the single-NW transport characterization were extracted from the growth substrate by sonicating in isopropyl alcohol and then drop-casted on top of a prepatterned *p*-GaAs substrate covered with a 200-nm SiO_2 layer. Single NWs were identified by SEM imaging, and the electrical contacts were fabricated by electron-beam lithography and evaporation of a Ni/Au/Ge/Au (5/5/30/200 nm) multilayer. Prior to metal evaporation, the exposed contact areas of GaAs NWs were treated with oxygen plasma to remove the residual resist, dipped in sequence in a $HCl:H_2O$ (1:10) solution for native oxide removal, and followed by a surface chemical passivation using $(NH_4)_2S_x$ (ammonium polysulfide) diluted in H_2O (15%, 45 °C, 3 min). Thermal annealing at 300 °C for 30 s was performed to improve the contact conductivity.

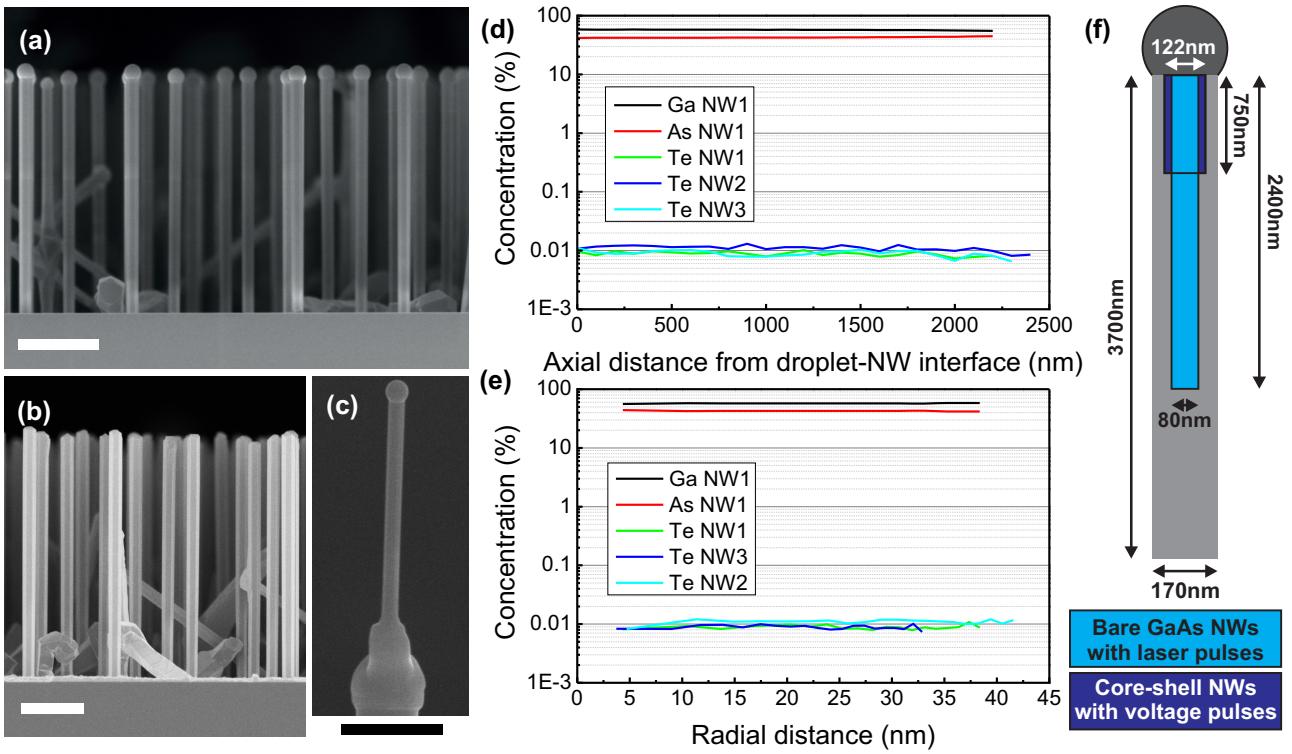

FIG. 1. Side-view SEM images of (a) bare Te-doped GaAs NWs and (b) core-shell NWs with Te-doped GaAs core and undoped AlGaAs shell. (c) 52° tilted SEM image of a single Te-doped GaAs NW placed on a Si post for APT investigation. (d) Axial and (e) radial atomic concentration profiles obtained for the bare GaAs NWs by APT using laser pulses. (f) Schematic illustration showing the dimensions of Te-doped GaAs NWs and the core region in the upper part of the NW from which the APT data were collected using laser pulses for the bare GaAs NWs and voltage pulses for core-shell NWs. The scale bars in (a)–(c) are 1 μm.

III. RESULTS AND DISCUSSION

A. Nanowire structure

Scanning electron microscope (SEM) images of Te-doped GaAs NWs and *n*-GaAs/*i*-AlGaAs core-shell NWs are shown in Figs. 1(a) and 1(b), respectively. It is clear that the Te-doped NWs exhibit remarkable size uniformity, which is typical for this growth method [26]. The average length and diameter of the bare Te-doped NWs grown for 60 min are 3700 and 170 nm, respectively. The undoped reference NWs grown for 60 min [Fig. S1(a) in the Supplemental Material [25]] have an average length and diameter of 4300 and 130 nm, respectively, indicating that the Te-doped NWs exhibit increased radial and decreased axial growth rates. This observation is consistent with the results reported in Refs. [17,19]. The undoped reference NWs grown for 80 min for the Raman experiments have an average length and diameter of 5100 and 150 nm, respectively [Fig. S1(b) in the Supplemental Material [25]]. The Te-doped NWs have zinc-blende crystal structure with rotational twinning defects (Figs. S2 and S3 in the Supplemental Material [25]). The twinning frequency increases toward the NW tip, where we observe the (111)-type sidewall faceting, reported previously for self-catalyzed Te-doped GaAs NWs grown on GaAs substrates [19].

B. Atom probe tomography

The concentration of Te atoms in GaAs NWs was investigated by APT, which involves evaporation of ions from the surface of NWs by a dc electric field, superposed with thermal pulses from laser or field pulses from a voltage pulser [27]. The evaporated ions are projected onto a detector [28,29]. In this paper, we used laser pulses for the bare Te-doped GaAs NWs and voltage pulses for core-shell NWs. APT analysis of the bare Te-doped GaAs NWs shows that they are homogeneously doped with $\sim 4 \times 10^{18}-\mathrm{cm}^{-3}$ Te throughout the volume imaged by APT [Fig. 1(f), [23,29,30]]. In addition, we detect trace amounts of P and Sb, which originate from the background flux in the MBE chamber. Figures 1(d) and 1(e) show the axial and radial atomic concentration profiles of Te in GaAs NWs. Note that the As deficiency in the APT analyses can be attributed to the counting errors originating from the formation of As ion clusters (such as As^{+} and $As_2{}^{++}$) that cannot be distinguished as they have the same mass-to-charge ratio.

As the field of view of atom probe tomography tools is limited to a solid angle covering about 1/8 of the sphere [23,29,30], ions are only collected from the inner part of the NWs as sketched in Fig. 1(f). In order to extend the field of view, we analyzed AlGaAs/GaAs core-shell NWs with nominally similar cores. Due to the projection artifacts during APT, as discussed in Ref. [24], only voltage pulsed APT analyses are possible on these structures. The corresponding results (Fig. S4 in the Supplemental Material [25]) are in a good agreement with the results obtained on bare GaAs NWs using laser pulses.

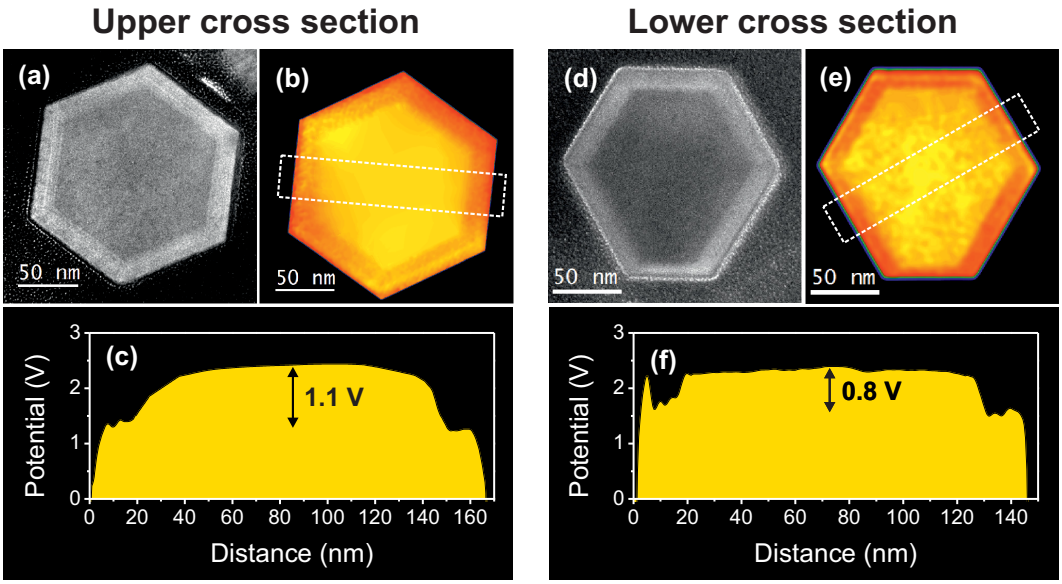

FIG. 2. Off-axis electron holography of cross-sectional slices extracted from the upper and lower sections of *n*-GaAs/*i*-AlGaAs core-shell NWs. (a), (d) Bright field TEM images of the slices. (b), (e) Potential maps of $V_{\mathrm{BI}} + \mathrm{MIP}$ extracted from the measured holographic phase maps using Eq. (2). (c), (f) Radial potential profiles taken from the dashed areas in (b) and (e), respectively.

C. Off-axis electron holography

APT gives the atomic concentration of dopants in the central part of the NW core and for the upper part of the NW. In order to investigate the distribution of activated dopants in more detail, we have conducted off-axis electron holography measurements for cross-sectional slices extracted from the upper and lower sections of *n*-GaAs/*i*-AlGaAs core-shell NWs. Electron holography is a transmission electron microscopy (TEM) technique which measures a spatially resolved phase difference, $\Delta\varphi$, by interference between electrons that pass through the specimen (object wave) and electrons that pass through vacuum (reference wave). The $\Delta\varphi$ is related to the crystal potential $V(x, y, z)$ according to

$$\Delta\varphi = C_E \int_0^H V(x, y, z)dz, \tag{1}$$

where C_E is a constant which depends on the microscope acceleration voltage and H is the specimen thickness. Electron holography has previously been used to measure the built-in potential (V_{BI}) and to assess the active doping in axial *p*-*n* junctions of Si NWs [31,32] and radial core-shell *p*-*i*-*n* junctions of GaAs NWs [20,33]. Assuming that the potential $V(x, y, z)$ is a sum of mean inner potential (MIP) and V_{BI}, and that they are both uniform in the z direction, we get

$$\Delta\varphi = C_E H(V_{\mathrm{BI}} + \mathrm{MIP}). \tag{2}$$

In the case of a heterogeneous core-shell structure, the difference in the MIP of the two materials has to be considered in order to estimate the correct V_{BI}. In this paper, the difference in the MIP between the GaAs core and the AlGaAs shell was estimated by using Vegard´s law, based on the composition values measured using the scanning transmission electron microscope in the energy-dispersive x-ray spectroscopy (STEM-EDX) mode, as discussed in the Supplemental Material [25].

Figure 2 shows the obtained results on slices cut from the upper and lower part of two NWs extracted from the same sample. The bright field TEM images of the upper and lower cross-sectional slices are shown in Figs. 2(a) and 2(d), respectively. In the BF-TEM images, the darker hexagonal core is GaAs and the brighter shell is AlGaAs. The slices were embedded in Pt, needed for protecting the NWs during the FIB cut.

The potential maps of $V_{\mathrm{BI}} + \mathrm{MIP}$ extracted from the measured holographic phase maps of the two cross-sectional samples are shown in Figs. 2(b) and 2(e). The potential profiles along the dashed areas are given in Figs. 2(c) and 2(f). From the STEM-EDX data, we know that the upper and lower slides have a slightly different shell composition, leading to different values of the MIP for the shell region in the upper and lower slices, respectively, as described in detail in Supplemental Material [25]. The differences in MIP between the core and the shell in the top and bottom part of the NW are given by

$$\Delta\mathrm{MIP}^{\mathrm{top}} = \mathrm{MIP}_{\mathrm{GaAs}} - \mathrm{MIP}^{\mathrm{top}}_{\mathrm{AlGaAs}} = 0.72\ \mathrm{V}, \tag{3}$$

$$\Delta\mathrm{MIP}^{\mathrm{bot}} = \mathrm{MIP}_{\mathrm{GaAs}} - \mathrm{MIP}^{\mathrm{bot}}_{\mathrm{AlGaAs}} = 0.53\ \mathrm{V}. \tag{4}$$

Using these values along with the measured potential steps in Figs. 2(c) and 2(f), we get built-in potentials $V_{\mathrm{BI}}^{\mathrm{top}} = 0.38\,\mathrm{V}$ and $V_{\mathrm{BI}}^{\mathrm{bot}} = 0.27\,\mathrm{V}$ for the top and bottom parts of the NW, respectively. Their difference equals $\Delta V_{\mathrm{BI}} = V_{\mathrm{BI}}^{\mathrm{top}} - V_{\mathrm{BI}}^{\mathrm{bot}} = 0.11$ V. This value will later be compared with a theoretical model. Now, we will investigate the dopant gradient using two complementary experimental techniques.

D. Raman spectroscopy

Single-NW micro-Raman spectroscopy allows us to probe the free-carrier density along the NW axis. The longitudinal optical (LO) plasmon mode couples with free carriers and forms a coupled phonon-plasmon mode (CPPM), which is sensitive to the charge carrier density and mobility [34–38].

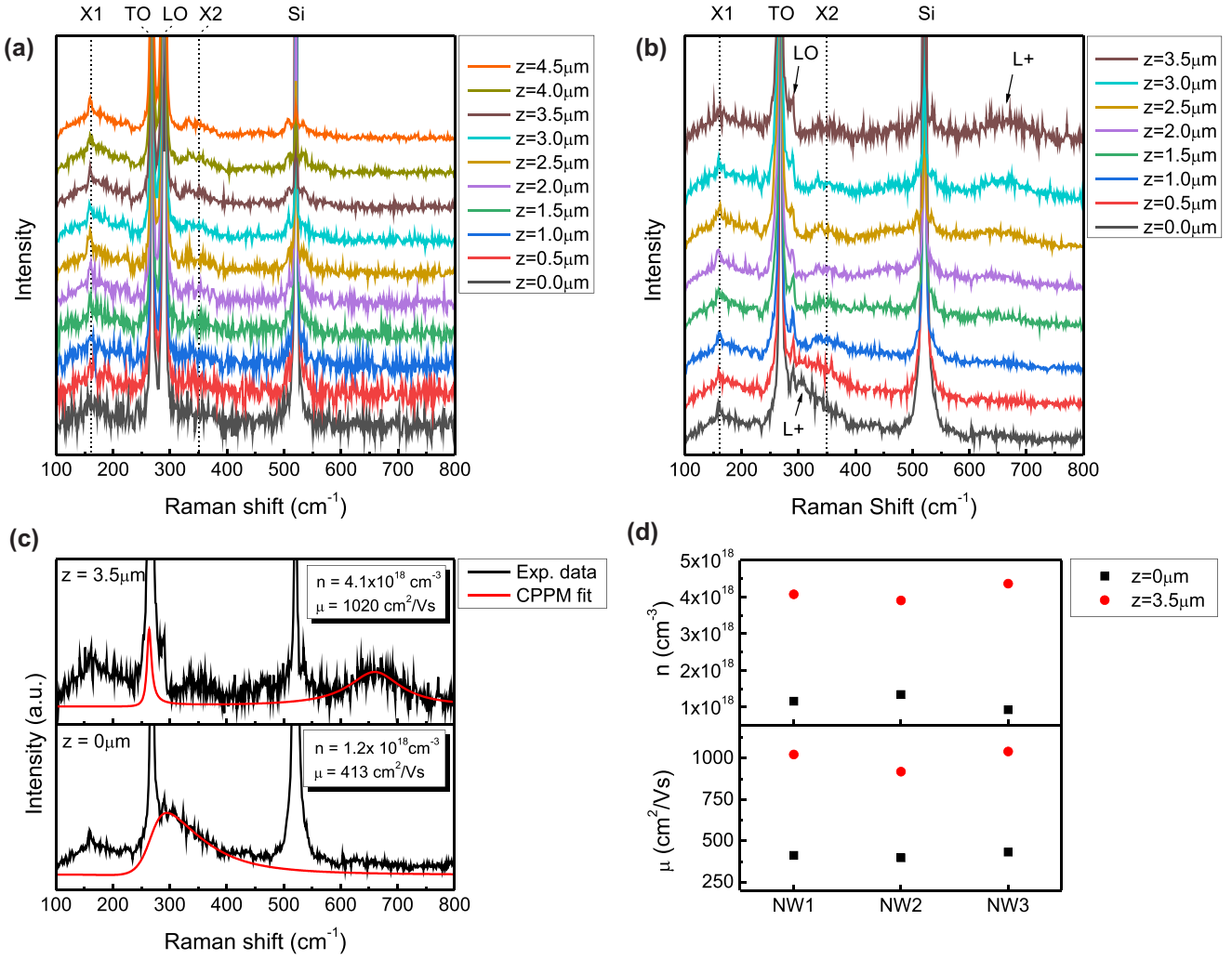

FIG. 3. Raman data obtained from individual vertical NWs by confocal z scans. (a) Raman spectra of an undoped reference NW at different focal positions. Positions at $z = 0$ and 4.5 μm correspond to the bottom and top of the undoped NW, respectively. (b) Raman spectra of Te-doped GaAs NW (NW1) at different focal positions. Positions at $z = 0$ and 3.5 μm correspond to the bottom and top of the NW, respectively. Raman spectra in (a) and (b) are normalized to the GaAs TO peak and offset vertically for illustrative purposes. (c) Experimental Raman data and CPPM fit by Eq. (5) for the top and bottom part of the Te-doped GaAs NW (NW1). The corresponding values of the electron concentration (n) and mobility (μ) are given in the insets. (d) Electron concentration and mobility data from the top and bottom parts of three different Te-doped GaAs NWs. The data for NW1 are from (c) and the data for NW2 and NW3 are from Fig. S9 in the Supplemental Material [25].

The shallow depth of focus of the Raman setup enabled probing the NWs along their vertical axis by adjusting the z-piezo position. Position $z = 0$ corresponds to the focus on the Si substrate (NW-substrate interface), and the focus moves towards the NW tip as the z value increases. Another benefit of this measurement configuration is that both TO and LO modes, as well as CPPM, are allowed in the (111) backscattering geometry [39]. The 80-min grown undoped NWs were used as the reference in the Raman experiments because their diameter is similar to that of Te-doped NWs.

The details of the GaAs LO and TO peaks, along with the Raman signal arising from the Si substrate, are presented in Fig. S8 in the Supplemental Material [25]. Here, we focus on the low intensity CPPM signal. Figure 3(a) shows the Raman spectra obtained from different axial positions for the undoped reference NWs, exhibiting typical GaAs TO and LO peaks. The peak related to the optical mode of the Si substrate is strongly suppressed as we move toward the upper part of the NW. In addition to these expected peaks, we observe broad features with X1 at 160 cm^{-1} and X2 at 350 cm^{-1}, most likely originating from disorder-activated acoustical phonons [40] and surface oxides [41–43]. Figure 3(b) shows the Raman spectra for a Te-doped GaAs NW, which exhibit two important differences with respect to the undoped reference. First, the intensity of the GaAs LO peak is greatly reduced, because the signal of uncoupled LO of doped NWs arises only from a surface depletion layer (which is thin for high doping densities [34–38]). Second, we observe the high-frequency branch of the CPPM mode (L+). In the lower part of the NW, the L+ branch is located on the higher-frequency side of the LO peak at around 300–350 cm^{-1}, shifting to 650–700 cm^{-1} as we move toward the NW tip.

CPPM line-shape analysis can be used for estimating free-carrier concentration, as shown in Refs. [44,45] for planar

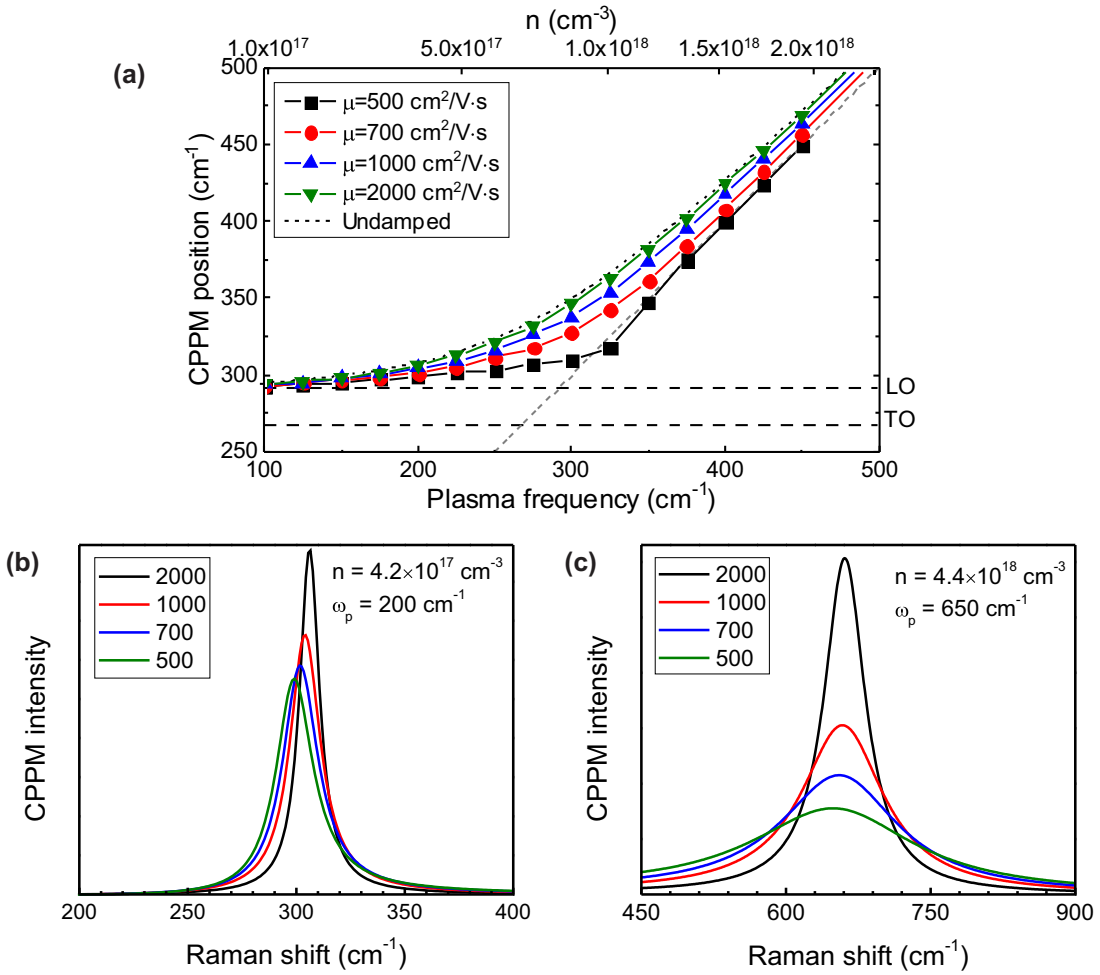

FIG. 4. (a) The position of the high-frequency (L+) branch of the CPPM mode calculated as a function of electron concentration using Eq. (5) for different values of electron mobility. The dashed gray line represents the plasma frequency and the dashed black line is the position of the CPPM mode in the undamped case [53]. (b), (c) Calculated CPPM line shapes for different values of electron mobility (in $\mathrm{cm}^2/\mathrm{V\,s}$) for electron concentrations of 4.2×10^{17} and $4.4 \times 10^{18}\ \mathrm{cm}^{-3}$, respectively.

layers and in Refs. [20,46–48] for NWs. The Raman scattering intensity of CPPM is given by [45]

$$I(\omega) = \frac{A\omega\Gamma_p\omega_p\left[\omega_{\mathrm{TO}}^2(1+C)-\omega^2\right]^2}{D}, \tag{5}$$

with

$$D = \left[\omega^2\left(\omega_{\mathrm{LO}}^2-\omega^2\right)-\omega_p^2\left(\omega_{\mathrm{TO}}^2-\omega^2\right)+\gamma\Gamma_p\omega^2\right]^2 + \left[\Gamma_p\omega\left(\omega_{\mathrm{LO}}^2-\omega^2\right)+\gamma\omega\left(\omega_p^2-\omega^2\right)\right]^2. \tag{6}$$

Here, ω_{TO} and ω_{LO} are the TO and LO frequencies, respectively, A is a frequency-independent parameter, $C = -0.49$ is the Faust-Henry coefficient for GaAs at room temperature for 532-nm laser excitation [49], and $\gamma = 5\,\mathrm{cm}^{-1}$ is the LO mode natural damping constant. The free-electron concentration n and mobility μ can be calculated from the plasma oscillation frequency of the free carriers $\omega_p^2 = ne^2/\epsilon_0\epsilon_\infty m_n^*$ and the damping constant $\Gamma_p = e/\mu m_e^*$, respectively, after fitting Eq. (5) to the experimental Raman data. The remaining symbols have the usual meanings: e is the elementary electron charge, $m_n^* = 0.079m_0$ the electron effective mass for n-GaAs [50], $\varepsilon_\infty = 10.86$ is the high-frequency dielectric constant for GaAs, and ε_0 is the vacuum permittivity.

We have fitted the CPPM peaks in Figs. 3(c) by Eq. (5), with different parameters for the upper and lower parts of the NWs. The resulting values of the electron concentration n and mobility μ for the upper and lower parts of three different Te-doped NWs are presented in Fig. 3(d). The reproducibility of the n and μ for different NWs is very good, and we consistently observe larger n in the top NW sections. Typically, μ should increase as n decreases, and therefore the observed relation of n and μ between the upper and lower part of the NWs is an unusual result which requires a careful interpretation. In Fig. 4 we show the position and line shape of the high-frequency (L+) branch of the CPPM mode calculated from Eq. (5) for the investigated range of n and μ. From Fig. 4(a) it is evident that the increase of n causes a rapid shift of the L+ peak, while the effect of mobility on the L+ peak position is significantly weaker. The reason for this is that, in the typical range of n-type mobilities for GaAs, we are approaching the undamped case where the damping constant Γ tends to zero. This is shown in

Fig. 4(a), which includes the theoretical CPPM peak position without damping. Therefore, the mobility has only a weak effect on the CPPM peak position in the investigated range of n and μ. On the other hand, the reduction of mobility strongly affects the broadening of the CPPM line shape, as shown in Figs. 4(b) and 4(c). Therefore, even a small overestimation of the L+ peak width in the fitting procedure would result in underestimation of μ, while not significantly affecting the resulting value of n. In the fitting procedure presented in Fig. 3(c) we expect an overestimation of the L+ width for the lower part of the NW due to overlapping of the CPPM mode with the X2 peak. For the upper part of the NW, we can obtain more reliable fitting because the L+ peak is spectrally isolated. It should be also noted that even a small inhomogeneity in the form of an axial or radial gradient of n in the volume probed in the Raman experiment will also lead to an overestimation of μ while not having significant effect on the resulting value of n. It has been shown also for p-type and n-type thin-film samples that while the Raman method produces accurate results for n in comparison to Hall data the values of μ tend to be less consistent due to different scattering mechanisms [51,52]. Consequently, we will take the results of the carrier concentration as the important output of the Raman experiments and conclude that a gradient in the carrier concentration is evident along the NW axis, as shown in Fig. 3, which is consistent with the holography results shown in Fig. 2. Remarkably, the electron concentration detected in the upper part of Te-doped NWs is $4 \times 10^{18}\,\mathrm{cm}^{-3}$, which matches with the Te atom concentration detected by APT in the same region. Thus, we can conclude that all Te donors are activated.

E. Transport characteristics

We further investigate the effect of Te doping on the NW transport characteristics by fabricating four evenly spaced electrodes on three individual NWs and measuring the current-voltage (I-V) characteristics between each contact pair in two-probe configuration. Figure 5(a) shows the typical I-V curves obtained from these experiments exhibiting nonlinear, asymmetric I-V characteristics. For each pair of contacts, the current is larger for positive than negative bias voltages, and higher currents are measured for the contacts closer to the tip of the NW than for those located closer to the bottom part.

In order to understand the I-V behavior, we need to consider the basic properties of n-GaAs-metal contacts which are characterized by formation of a Schottky contact with the barrier determined by Fermi level pinning at the GaAs surface regardless of the work function of the metal. The barrier heights for common metals such as Cu, Pd, Ag, Au, Al, Ni, and Sn on the n-GaAs(110) surface result in barrier heights in the range from 0.7 to 0.9 eV [54]. The mechanism of current transport through such interfaces depends on the doping level. At low to moderate doping concentrations the current is due to thermionic emission (TE) over the barrier, resulting in typical Schottky diode behavior with saturation of the reverse current. Linear I-V characteristics and low contact resistance associated to Ohmic contacts are obtained in the case of high doping concentrations, which leads to the reduction of the barrier width. This allows field emission

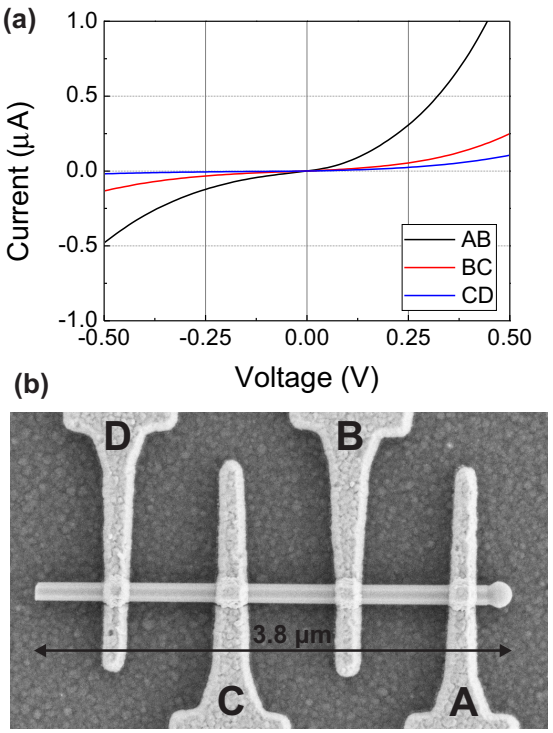

FIG. 5. (a) Asymmetric double-Schottky-type I-V curves measured for a Te-doped GaAs NW using different contact pairs as indicated in (b).

(FE), i.e., tunneling of electrons with energies close to the Fermi energy in the semiconductor, through the barrier. In the intermediate doping regime the barrier is too wide to allow tunneling at the Fermi energy and thus the primary mechanism is thermionic field emission (TFE), which involves tunneling of thermally excited electrons through the narrower upper part of the barrier. [55,56]

The I–V curves in Fig. 5(a) can be understood as a result of back-to-back Schottky contacts separated by the section of the NW as a resistive channel. One of the contacts is reverse biased and the other forward biased depending on the polarity of the bias voltage. The resistive voltage drop in the semiconductor channel between two contacts can be estimated as $U = RI$, where the resistance $R = L/en\mu A$. For the NW in Fig. 5 we use a channel length of $L = 700\,\mathrm{nm}$ and an area A of a hexagonal cross section with a diameter of 160 nm. In the upper part of the NW we have $n = 4 \times 10^{18}\,\mathrm{cm}^{-3}$ and $\mu = 1000\,\mathrm{cm}^2/\mathrm{V\,s}$, as determined by Raman, which results in $U = 0.3\,\mathrm{mV}$ for 0.5-μA current at 0.5-V bias voltage. Similarly for the bottom part having $n = 1 \times 10^{18}\,\mathrm{cm}^{-3}$ and $\mu = 400\,\mathrm{cm}^2/\mathrm{V\,s}$, we get $U = 3\,\mathrm{mV}$. The voltage drop in the NW channel is more than two orders of magnitude smaller than the applied bias. Therefore, it is reasonable to consider that the current flow is predominantly limited by the reverse-biased Schottky contact even assuming a considerable error margin for the values of μ obtained from Raman, in particular since the value of μ from Raman is more likely to be underestimated than overestimated. In Fig. 5(a), higher currents for each contact pair are observed when the contact closer to the tip of the NW is reverse biased. The reverse leakage current

increases when we move from the bottom of the NW (contact D) towards the tip (contact A).

In the Supplemental Material Sec. VII and Fig. S11 [25] we assess the primary current transport mechanisms under reverse bias for different temperature, carrier concentration, and bias ranges using the formulation by Padovani and Stratton [55]. For room temperature and the range of doping levels observed in APT and Raman, the reverse current through the contact between the investigated Te-doped NWs and metal contacts is primarily due to TFE, while for the upper part of the NW which has higher doping level there is a probability of pure FE in the higher range of the bias voltages. The reverse current increases with carrier concentration in both TFE and FE due to narrowing of the barrier width. Therefore, the I-V characteristics shown in Fig. 5(a) indicate the presence of dopant gradient along the NW axis.

It should be noted that the magnitude of the reverse current through a Schottky junction depends on the interface properties by multiple mechanisms including voltage-dependent barrier reduction due to image force, effect of GaAs surface termination on the Fermi level pinning position, defect assisted tunneling, and the presence of thin interface layers [56]. However, the reverse leakage current is nevertheless dependent on the doping level, allowing qualitative assessment of dopant gradient along the NW given that there is no significant difference in the interface properties between different contacts (A-D). In order to exclude the possibility of random variations in NW growth and device processing, we measured multiple devices which all show a similar trend with higher reverse leakage for the contacts located closer to the NW tip (Fig. S10 in the Supplemental Material [25]).

These results indicate the presence of a dopant gradient which increases in the axial direction from the bottom to the tip of the NW, which is consistent with off-axis electron holography and Raman results. It should be noted that in the transport measurements we observe a significant difference between reverse leakage currents of contacts A and B at the upper part of the NW, while APT shows a uniform Te concentration throughout the upper part of the NW in the core region (Fig. 1). This can be explained by the presence of both axial and radial dopant concentration gradients and the fact that APT probes the NW core while the I-V characteristics depend more on the doping level in the surface layer.

IV. MODEL FOR Te INCORPORATION

The data presented in Figs. 1 –5 provide several indications of doping gradients in Te-doped GaAs NWs. While the APT data reveal a relatively uniform Te concentration in the core region in the upper part of the NWs, we observe a higher V_{BI} in the upper than in the lower cross section of n-GaAs/i-AlGaAs core-shell NWs. Furthermore, the Raman data show an increasing free-carrier concentration toward the NW top, and a similar trend is detected from the transport measurements.

Therefore, it is reasonable to assume that Te atoms incorporate into the solid NW through the Ga droplet by the VLS mechanism, leading to a relatively uniform dopant concentration in each newly formed monolayer. Under Ga-rich conditions used for Ga-catalyzed growth of GaAs NWs, the droplet radius gradually increases toward the NW top [57–59]. However, the observed shape of our NWs is straight from base to top rather than reverse tapered. This straight NW morphology should be due to the radial VS growth of a GaAs shell around the initially tapered core, as in Refs. [58,59]. The dopant incorporation through the NW sidewalls by the VS mechanism has been shown to be insignificant in the case of Be-doped self-catalyzed GaAs NWs [33]. Similar behavior can be expected for Te, particularly due to its high vapor pressure which leads to a strong temperature dependence of the incorporation probability at the sidewalls [60]. Hence, the GaAs shell should be initially undoped. A gradient of the Te concentration between the doped core and the undoped shell gives rise to solid diffusion of Te into the shell. Very importantly, the amount of Te incorporated through the droplet is proportional to the squared radius of the droplet base, which equals the NW core radius. Therefore, less Te atoms incorporate into a thinner NW bottom than to a thicker top. This explains why the average Te concentration in the top cross section exceeds the one in the bottom part of the same NW. Possible diffusion of Te from the GaAs region into the undoped AlGaAs shell layer is considered negligible because of the low temperature employed to grow AlGaAs. These considerations lead to the growth model illustrated in Fig. 6(a), where we only consider the doping profiles in GaAs.

Within the model, the initial Te concentration in a new monolayer having the area $\Omega(t)$ at the moment of time t is considered spatially uniform and independent of the height z, that is, $C(x, y, z, t) = C_0$ if the point (x, y) belongs to $\Omega(t)$. Subsequent evolution of the Te concentration is described by the nonstationary diffusion equation

$$\frac{\partial C(x, y, t)}{\partial t} = D \cdot \nabla^2 C(x, y, t), \tag{7}$$

with the initial condition $C(x, y, t = 0) = C_0$. Here, D denotes the diffusion coefficient of Te atoms in solid GaAs. The boundary condition corresponds to zero vapor-solid influx across the NW core boundary S:

$$\left.\frac{\partial C(x, y, t)}{\partial \vec{n}}\right|_S = 0, \tag{8}$$

where $\vec{n}$ is the normal to the boundary.

In order to find the unknown C_0, we note that the total number of Te atoms N arriving into the droplet seated on top of a NW having the radius R_b (defined as the distance from the NW axis to the corner of the NW hexagon) during the period of time Δt of forming the monolayer is given by

$$N = \varphi(\beta) I \pi R_b^2 \Delta t. \tag{9}$$

Here, $\varphi(\beta)$ is a geometrical coefficient which depends on the droplet contact angle β and I is the effective atomic flux of Te atoms. The Te concentration in the core immediately after the monolayer formation equals $C_0 = N/V$, where V is the monolayer volume. Using Eq. (9) and $V = 3\sqrt{3}R_b^2 h/2$, with h as the monolayer height, C_0 takes the form

$$C_0 = \frac{2\pi\varphi(\beta) I}{3\sqrt{3} v_L}, \tag{10}$$

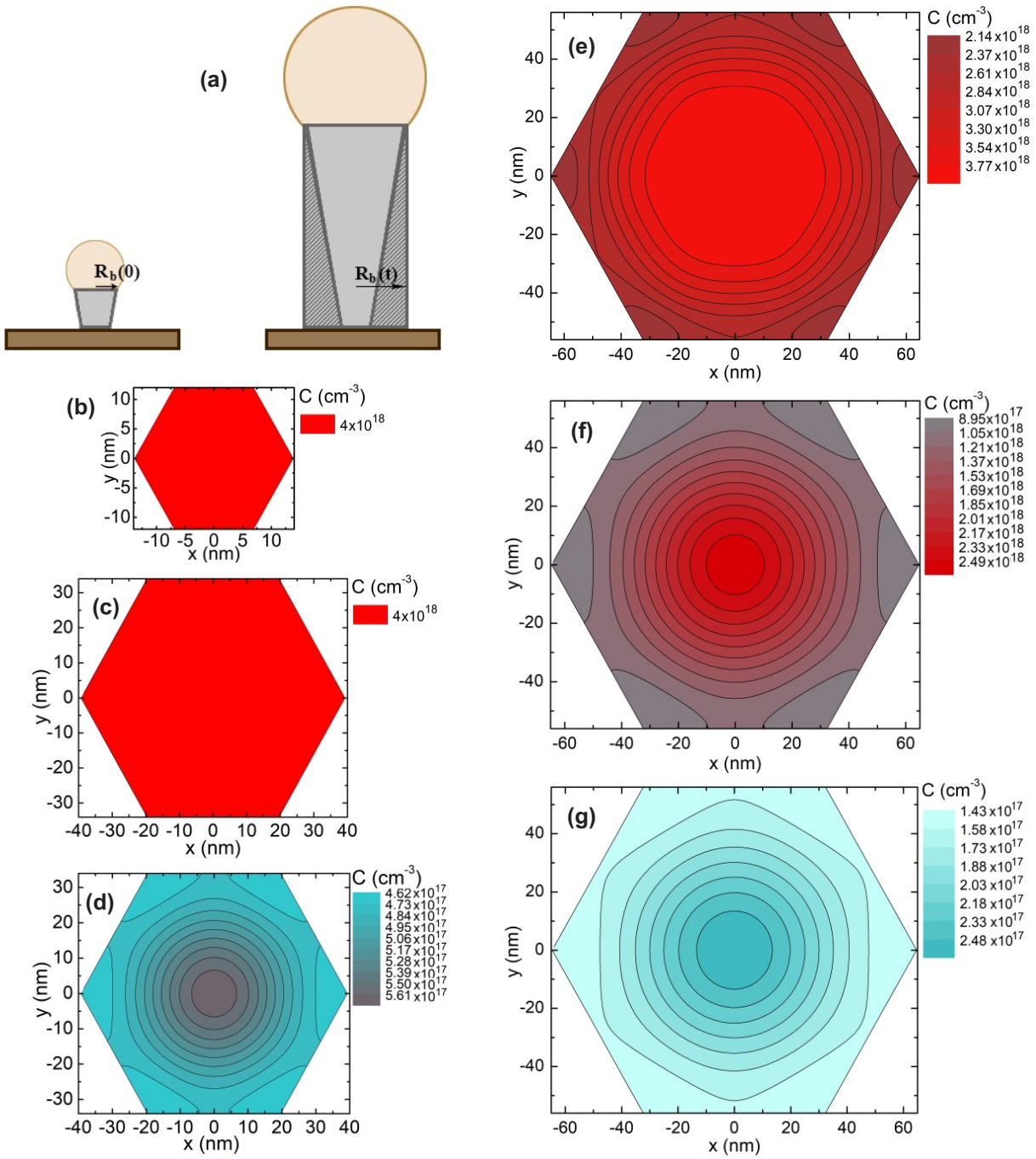

FIG. 6. (a) Growth model of Ga-catalyzed GaAs NWs under Ga-rich conditions. The shaded segments show the shell that forms by the VS mechanism around the reverse tapered VLS core. The NW radius at a given height increases from its initial value $R_b(0)$ to $R_b(t)$ over the period of time t. Te doping profiles at different moments of time: (b) $t = 0$ s; $t = 1500$ s at (c) the center and (d) bottom part of the NW; $t = 3000$ s at (e) 500 nm below the NW tip, (f) center part, and (g) bottom part of the NW.

where $v_L = h/\Delta t$ is the axial NW growth rate. The average concentration $\bar{C}_{\rm bot}(t_c)$ upon the completion of the NW core (say, at $t = t_c$) is proportional to the ratio of the initial over the final NW cross-sectional area:

$$\bar{C}_{\rm bot} = \frac{2\pi\varphi(\beta)}{3\sqrt{3}v_L}\left(\frac{R_b(0)}{R_b(t_c)}\right)^2. \tag{11}$$

The built-in potential of a *p*-*n* junction is given by [32]

$$V_{\rm BI} = \frac{k_B T}{e}\ln\left(\frac{N_A^- N_D^+}{n_i^2}\right), \tag{12}$$

where N_D^+ is the ionized dopant concentration which simply equals $C(x, y, z, t)$, N_A^- is the ionized acceptor concentration, n_i is the intrinsic carrier concentration, e is the electron charge,

k_B is the Boltzmann constant, and T is room temperature. Clearly, the difference of the built-in potentials at the NW top and bottom is due to the difference in average Te concentrations in the two cross sections, which equals

$$\Delta V_{\mathrm{BI}} = \frac{k_B T}{e} \ln\left(\frac{N_D^{+\mathrm{top}}}{N_D^{+\mathrm{bot}}}\right). \tag{13}$$

Using Eq. (12) and $C_{\mathrm{top}} = C_0$, this can be put as

$$\Delta V_{\mathrm{BI}} = \frac{k_B T}{e} \ln\left(\frac{R_b(t_c)}{R_b(0)}\right)^2. \tag{14}$$

The difference of the built-in potentials at the NW top and bottom for a NW with the initial radius $R_b(0) = 14$ nm, which is relevant for these growth conditions [26], and the final radius of $R_b(t_c) = 65$ nm equals $\Delta V_{\mathrm{BI}} \approx 0.1$ eV. The obtained value is in good agreement with the experimental data obtained from off-axis electron holography.

Figures 6(b)–6(g) show the time evolution of the dopant distribution obtained numerically for the bottom, center, and top sections of the NW at different growth times—0 s ($R_b =$ 14 nm), 1500 s ($R_b = 34$ nm), and 3000 s ($R_b = 65$ nm) using a diffusion coefficient of $D = 0.2\,\mathrm{nm}^2/\mathrm{s}$, which is within the previously reported range [61,62]. Comparing Figs. 6(e)–6(g), the radial gradient for the upper slice is slightly larger than for the lower one, which agrees with the holography potential profiles [see Figs. 2(c) and 2(f)]. It should be noted that the radial gradient depends on the ratio of the diffusion coefficient over the radial growth rate. Hence, fast diffusion leads to the uniform dopant distribution, whereas fast radial growth results in a significant doping inhomogeneity. This shows the importance of the growth conditions in controllable Te doping of self-catalyzed GaAs NWs.

V. CONCLUSIONS

In conclusion, by combining a large amount of data from complementary experimental techniques and a theoretical model, we have shown that Te dopants incorporate in self-catalyzed GaAs NWs via the VLS mechanism through the Ga droplet. Such incorporation process results in both axial and radial doping gradients when radial VS growth and diffusion of Te in solid GaAs are present. Consequently, careful control of growth conditions is required for obtaining uniform doping throughout the NW. Our model identifies fast radial growth of GaAs by step flow at the sidewalls of GaAs NWs as the key factor for the observed doping inhomogeneity. Therefore, certain improvements of the VLS growth protocols are required to achieve more homogeneous Te doping. In particular, the radial growth of self-catalyzed III-V NWs can be suppressed by increasing the V/III flux ratio as described in Refs. [59,63,64]. We plan to investigate this problem in future work. Remarkably, our data for the free-electron concentration from Raman spectroscopy and Te-dopant concentration from APT in the upper part of the NW show that 100% activation of Te dopants can be achieved at a doping level of $4 \times 10^{18}\,\mathrm{cm}^{-3}$, which is extremely promising for device applications using Te as an n-type dopant of GaAs NWs.

ACKNOWLEDGMENTS

This work made use of Tampere Microscopy Center facilities at Tampere University. T.H., M.R.P., E.K., and M.G. acknowledge financial support from the Academy of Finland Project NESP (Grant No. 294630) and NanoLight (Grant No. 310985). M.R.P. acknowledges CAPES/CNPq Grant No. 88887.100549/2015-00. Y.G.G. and H.V.A.G. acknowledge financial support from Fundação de Amparo a Pesquisa do Estado de São Paulo (Grants No. 18/01808-5, No. 16/10668-7, and No. 14/50513-7). V.G.D. gratefully acknowledges the financial support of the Russian Foundation for Basic Research under Grants No. 17-52-16017, No. 18-02-40006, and No. 19-52-53031.

[1] A. Zhang, G. Zheng, and C. M. Lieber, *Nanowires: Building Blocks for Nanoscience and Nanotechnology* (Springer, New York, 2016).

[2] C. Colombo, D. Spirkoska, M. Frimmer, G. Abstreiter, and A. Fontcuberta i Morral, Ga-assisted catalyst-free growth mechanism of GaAs nanowires by molecular beam epitaxy, Phys. Rev. B **77**, 155326 (2008).

[3] F. Jabeen, V. Grillo, S. Rubini, and F. Martelli, Self-catalyzed growth of GaAs nanowires on cleaved Si by molecular beam epitaxy, Nanotechnology **19**, 275711 (2008).

[4] W. Bullis, Properties of gold in silicon, Solid State Electron. **9**, 143 (1966).

[5] E. Dimakis, U. Jahn, M. Ramsteiner, A. Tahraoui, J. Grandal, X. Kong, O. Marquardt, A. Trampert, H. Riechert, and L. Geelhaar, Coaxial multishell (In, Ga) As/GaAs nanowires for near-infrared emission on Si substrates, Nano Lett. **14**, 2604 (2014).

[6] C. P. T. Svensson, T. Mårtensson, J. Trägårdh, C. Larsson, M. Rask, D. Hessman, L. Samuelson, and J. Ohlsson, Monolithic GaAs/InGaP nanowire light emitting diodes on silicon, Nanotechnology **19**, 305201 (2008).

[7] I. Åberg, G. Vescovi, D. Asoli, U. Naseem, J. P. Gilboy, C. Sundvall, A. Dahlgren, K. E. Svensson, N. Anttu, and M. T. Björk, A GaAs nanowire array solar cell with 15.3% efficiency at 1 sun, IEEE Journal of Photovoltaics **6**, 185 (2016).

[8] D. van Dam, N. J. van Hoof, Y. Cui, P. J. van Veldhoven, E. P. Bakkers, J. Gómez Rivas, and J. E. Haverkort, High-efficiency nanowire solar cells with omnidirectionally enhanced absorption due to self-aligned indium-tin-oxide Mie scatterers, ACS nano **10**, 11414 (2016).

[9] M. D. Thompson, A. Alhodaib, A. P. Craig, A. Robson, A. Aziz, A. Krier, J. Svensson, L. Wernersson, A. M. Sanchez, and A. R. Marshall, Low leakage-current InAsSb nanowire photodetectors on silicon, Nano Lett. **16**, 182 (2015).

[10] S. A. Dayeh, R. Chen, Y. G. Ro, and J. Sim, Progress in doping semiconductor nanowires during growth, Mater. Sci. Semicond. Process. **62**, 135 (2017).

[11] E. Dimakis, M. Ramsteiner, A. Tahraoui, H. Riechert, and L. Geelhaar, Shell-doping of GaAs nanowires with Si for n-type conductivity, Nano Res. **5**, 796 (2012).

[12] B. Ketterer, E. Mikheev, E. Uccelli, and A. Fontcuberta i Morral, Compensation mechanism in silicon-doped gallium arsenide nanowires, Appl. Phys. Lett. **97**, 223103 (2010).

[13] E. F. Schubert, *Doping in III-V Semiconductors* (Cambridge University, Cambridge, England, 1993).

[14] J. De-Sheng, Y. Makita, K. Ploog, and H. Queisser, Electrical properties and photoluminescence of Te-doped GaAs grown by molecular beam epitaxy, J. Appl. Phys. **53**, 999 (1982).

[15] T. Orzali, A. Vert, R. T. Lee, A. Norvilas, G. Huang, J. L. Herman, R. J. Hill, and S. S. P. Rao, Heavily tellurium doped n-type InGaAs grown by MOCVD on 300 mm Si wafers, J. Cryst. Growth **426**, 243 (2015).

[16] M. Yano, Y. Suzuki, T. Ishii, Y. Matsushima, and M. Kimata, Molecular beam epitaxy of GaSb and $GaSb_xAs_{1-x}$, Japan. J. Appl. Phys. **17**, 2091 (1978).

[17] J. A. Czaban, D. A. Thompson, and R. R. LaPierre, GaAs core-shell nanowires for photovoltaic applications, Nano Lett. **9**, 148 (2008).

[18] O. Salehzadeh, M. Chen, K. Kavanagh, and S. Watkins, Rectifying characteristics of Te-doped GaAs nanowires, Appl. Phys. Lett. **99**, 182102 (2011).

[19] S. Suomalainen, T. Hakkarainen, T. Salminen, R. Koskinen, M. Honkanen, E. Luna, and M. Guina, Te-doping of self-catalyzed GaAs nanowires, Appl. Phys. Lett. **107**, 012101 (2015).

[20] N. I. Goktas, E. M. Fiordaliso, and R. LaPierre, Doping assessment in GaAs nanowires, Nanotechnology **29**, 234001 (2018).

[21] M. Orrù, E. Repiso, S. Carapezzi, A. Henning, S. Roddaro, A. Franciosi, Y. Rosenwaks, A. Cavallini, F. Martelli, and S. Rubini, A roadmap for controlled and efficient n-type doping of self-assisted GaAs nanowires grown by molecular beam epitaxy, Adv. Funct. Mater. **26**, 2836 (2016).

[22] T. Hakkarainen, A. Schramm, J. Mäkelä, P. Laukkanen, and M. Guina, Lithography-free oxide patterns as templates for self-catalyzed growth of highly uniform GaAs nanowires on Si (111), Nanotechnology **26**, 275301 (2015).

[23] S. Koelling, A. Li, A. Cavalli, S. Assali, D. Car, S. Gazibegovic, E. Bakkers, and P. Koenraad, Atom-by-atom analysis of semiconductor nanowires with parts per million sensitivity, Nano Lett. **17**, 599 (2017).

[24] S. Koelling, R. C. Plantenga, H. I. Hauge, Y. Ren, A. Li, M. A. Verheijen, S. C. Boj, S. Assali, P. M. Koenraad, and E. P. Bakkers, Impurity and defect monitoring in hexagonal Si and SiGe nanocrystals, ECS Trans. **75**, 751 (2016).

[25] See Supplemental Material at http://link.aps.org/supplemental/10.1103/PhysRevMaterials.3.086001 for SEM micrographs of undoped reference NWs; TEM images of Te-doped GaAs NWs; APT of core-shell NWs using voltage pulses; determination of AlGaAs shell composition by EDX; additional Raman data for undoped and Te-doped GaAs NWs; additional current-voltage data for Te-doped GaAs NWs; and evaluation of the primary current transport mechanism under reverse bias.

[26] E. S. Koivusalo, T. V. Hakkarainen, M. D. Guina, and V. G. Dubrovskii, Sub-Poissonian narrowing of length distributions realized in Ga-catalyzed GaAs nanowires, Nano Lett. **17**, 5350 (2017).

[27] T. F. Kelly and D. J. Larson, Atom probe tomography 2012, Annu. Rev. Mater. Res. **42**, 1 (2012).

[28] R. G. Forbes, Field evaporation theory: A review of basic ideas, Appl. Surf. Sci. **87–88**, 1 (1995).

[29] P. Bas, A. Bostel, B. Deconihout, and D. Blavette, A general protocol for the reconstruction of 3D atom probe data, Appl. Surf. Sci. **87–88**, 298 (1995).

[30] B. Geiser, D. Larson, E. Oltman, S. Gerstl, D. Reinhard, T. Kelly, and T. Prosa, Wide-field-of-view atom probe reconstruction, Microsc. Microanal. **15**, 292 (2009).

[31] M. I. den Hertog, H. Schmid, D. Cooper, J. Rouviere, M. T. Björk, H. Riel, P. Rivallin, S. Karg, and W. Riess, Mapping active dopants in single silicon nanowires using off-axis electron holography, Nano Lett. **9**, 3837 (2009).

[32] Z. Gan, D. E. Perea, J. Yoo, S. Tom Picraux, D. J. Smith, and M. R. McCartney, Mapping electrostatic profiles across axial pn junctions in Si nanowires using off-axis electron holography, Appl. Phys. Lett. **103**, 153108 (2013).

[33] M. H. T. Dastjerdi, E. M. Fiordaliso, E. Leshchenko, A. Akhtari-Zavareh, T. Kasama, M. Aagesen, V. G. Dubrovskii, and R. R. LaPierre, Three-fold symmetric doping mechanism in GaAs nanowires, Nano Lett. **17**, 5875 (2017).

[34] G. Abstreiter, R. Trommer, M. Cardona, and A. Pinczuk, Coupled plasmon-LO phonon modes and Lindhard-Mermin dielectric function of n-GaAs, Solid State Commun. **30**, 703 (1979).

[35] B. Tell and R. Martin, Raman scattering by coupled optical-phonon-plasmon modes in GaAs, Phys. Rev. **167**, 381 (1968).

[36] A. Mooradian and G. Wright, Observation of the Interaction of Plasmons with Longitudinal Optical Phonons in GaAs, Phys. Rev. Lett. **16**, 999 (1966).

[37] C. Olson and D. W. Lynch, Longitudinal-optical-phonon-plasmon coupling in GaAs, Phys. Rev. **177**, 1231 (1969).

[38] S. Katayama and K. Murase, Raman scattering by coupled LO phonon-plasmon mode in n-GaAs, J. Phys. Soc. Jpn. **42**, 886 (1977).

[39] J. Steele, P. Puech, and R. A. Lewis, Polarized Raman backscattering selection rules for (hhl)-oriented diamond-and zincblende-type crystals, J. Appl. Phys. **120**, 055701 (2016).

[40] A. M. Mintairov, P. A. Blagnov, V. G. Melehin, N. N. Faleev, J. L. Merz, Y. Qiu, S. A. Nikishin, and H. Temkin, Ordering effects in Raman spectra of coherently strained $GaAs_{1-x}N_x$, Phys. Rev. B **56**, 15836 (1997).

[41] R. L. Farrow, R. K. Chang, S. Mroczkowski, and F. H. Pollak, Detection of excess crystalline As and Sb in III-V oxide interfaces by Raman scattering, Appl. Phys. Lett. **31**, 768 (1977).

[42] L. G. Quagliano, Detection of As2O3 arsenic oxide on GaAs surface by Raman scattering, Appl. Surf. Sci. **153**, 240 (2000).

[43] S. Yazji, I. Zardo, M. Soini, P. Postorino, A. F. i Morral, and G. Abstreiter, Local modification of GaAs nanowires induced by laser heating, Nanotechnology **22**, 325701 (2011).

[44] G. Irmer, M. Wenzel, and J. Monecke, Light scattering by a multicomponent plasma coupled with longitudinal-optical phonons: Raman spectra of *p*-type GaAs: Zn, Phys. Rev. B **56**, 9524 (1997).

[45] A. Mlayah, R. Carles, G. Landa, E. Bedel, and A. Muñoz-Yagüe, Raman study of longitudinal optical phonon-plasmon

coupling and disorder effects in heavily Be-doped GaAs, J. Appl. Phys. **69**, 4064 (1991).

[46] F. Amaduzzi, E. Alarcón-Lladó, H. Hautmann, R. Tanta, F. Matteini, G. Tütüncüoğlu, T. Vosch, J. Nygård, T. Jespersen, and E. Uccelli, Tuning the response of non-allowed Raman modes in GaAs nanowires, J. Phys. D **49**, 095103 (2016).

[47] B. Ketterer, E. Uccelli, and A. F. i Morral, Mobility and carrier density in p-type GaAs nanowires measured by transmission Raman spectroscopy, Nanoscale **4**, 1789 (2012).

[48] A. Casadei, P. Krogstrup, M. Heiss, J. A. Röhr, C. Colombo, T. Ruelle, S. Upadhyay, C. B. Sørensen, J. Nygård, and A. Fontcuberta i Morral, Doping incorporation paths in catalyst-free Be-doped GaAs nanowires, Appl. Phys. Lett. **102**, 013117 (2013).

[49] S. Zekeng, B. Prevot, and C. Schwab, Raman determination of the Faust-Henry coefficient of GaAs in the 1.9 to 2.7 eV range at ordinary and low temperatures, Phys. Status Solidi B **150**, 65 (1988).

[50] A. Raymond, J. Robert, and C. Bernard, The electron effective mass in heavily doped GaAs, J. Phys. C **12**, 2289 (1979).

[51] G. Irmer, V. Toporov, B. Bairamov, and J. Monecke, Determination of the charge carrier concentration and mobility in n-gap by Raman spectroscopy, Phys. Status Solidi B **119**, 595 (1983).

[52] G. Irmer, W. Siegel, G. Kuhnel, J. Monecke, F. Yasuoka, B. Bairamov, and V. Toporov, Determination of the hole concentration and mobility of p-GaP by Hall and by Raman measurements, Semicond. Sci. Technol. **6**, 1072 (1991).

[53] B. B. Varga, Coupling of plasmons to polar phonons in degenerate semiconductors, Phys. Rev. **137**, A1896 (1965).

[54] N. Newman, M. van Schilfgaarde, T. Kendelwicz, M. D. Williams, and W. E. Spicer, Electrical study of Schottky barriers on atomically clean GaAs (110) surfaces, Phys. Rev. B **33**, 1146 (1986).

[55] F. Padovani and R. Stratton, Field and thermionic-field emission in Schottky barriers, Solid State Electron. **9**, 695 (1966).

[56] E. H. Rhoderic and R. H. Williams, *Metal-Semiconductor Contacts*, 2nd ed. (Caledon, Oxford, 1988).

[57] P. Kuyanov, J. Boulanger, and R. LaPierre, Control of GaP nanowire morphology by group V flux in gas source molecular beam epitaxy, J. Cryst. Growth **462**, 29 (2017).

[58] G. Priante, S. Ambrosini, V. G. Dubrovskii, A. Franciosi, and S. Rubini, Stopping and resuming at will the growth of GaAs nanowires, Crystal Growth & Design **13**, 3976 (2013).

[59] W. Kim, V. G. Dubrovskii, J. Vukajlovic-Plestina, G. Tütüncüoglu, L. Francaviglia, L. Güniat, H. Potts, M. Friedl, J. Leran, and A. Fontcuberta i Morral, Bistability of contact angle and its role in achieving quantum-thin self-assisted GaAs nanowires, Nano Lett. **18**, 49 (2017).

[60] D. M. Collins, J. Miller, Y. G. Chai, and R. Chow, Sn and Te doping of molecular beam epitaxial GaAs using a SnTe source, J. Appl. Phys. **53**, 3010 (1982).

[61] W. Chen, V. G. Dubrovskii, X. Liu, T. Xu, R. Lardé, J. Philippe Nys, B. Grandidier, D. Stiévenard, G. Patriarche, and P. Pareige, Boron distribution in the core of Si nanowire grown by chemical vapor deposition, J. Appl. Phys. **111**, 094909 (2012).

[62] E. Koren, N. Berkovitch, and Y. Rosenwaks, Measurement of active dopant distribution and diffusion in individual silicon nanowires, Nano Lett. **10**, 1163 (2010).

[63] V. G. Dubrovskii, Group V sensitive vapor-liquid-solid growth of Au-catalyzed and self-catalyzed III-V nanowires, J. Cryst. Growth **440**, 62 (2016).

[64] E. Leshchenko, P. Kuyanov, R. LaPierre, and V. Dubrovskii, Tuning the morphology of self-assisted GaP nanowires, Nanotechnology **29**, 225603 (2018).